REPORT DOCUMENTATION PAGE

1. REPORT DATE *(DD-MM-YYYY)*	2. REPORT TYPE	3. DATES COVERED *(From - To)*

4. TITLE AND SUBTITLE

5a. CONTRACT NUMBER

5b. GRANT NUMBER

5c. PROGRAM ELEMENT NUMBER

6. AUTHOR(S)

5d. PROJECT NUMBER

5e. TASK NUMBER

5f. WORK UNIT NUMBER

7. PERFORMING ORGANIZATION NAME(S) AND ADDRESS(ES)

8. PERFORMING ORGANIZATION REPORT NUMBER

9. SPONSORING/MONITORING AGENCY NAME(S) AND ADDRESS(ES)

10. SPONSOR/MONITOR'S ACRONYM(S)

11. SPONSOR/MONITOR'S REPORT NUMBER(S)

12. DISTRIBUTION/AVAILABILITY STATEMENT

13. SUPPLEMENTARY NOTES

14. ABSTRACT

15. SUBJECT TERMS

16. SECURITY CLASSIFICATION OF:			17. LIMITATION OF ABSTRACT	18. NUMBER OF PAGES	19a. NAME OF RESPONSIBLE PERSON
a. REPORT	b. ABSTRACT	c. THIS PAGE			
					19b. TELEPHONE NUMBER *(Include area code)*

Final Report
from

Rochester Institute of Technology
Physics Department
85 Lomb Memorial Drive
Rochester, NY 14623

to
Air Force Office of Scientific Research
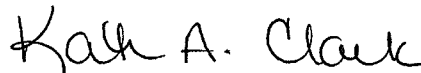ATTN: Dr. Kitt Reinhardt
USAF AFMC AFOSR/NE

Title:

Understanding / Modeling of Thermal and Radiation Benefits of Quantum Dot Solar Cells

Principal Investigator

Dr. Ryne P. Raffaelle
Associate Professor of Physics
(585) 475 – 5149
email: rprsps@rit.edu

Authorized Representative
To Conduct Negotiations

Katherine A. Clark
Grants and Accounting
(585) 475 - 7984

Date: July 11, 2008

Summary

The radiation and thermal dependence of strain compensated InAs QD / GaAs solar cells have been investigated. Strain compensation is a key step in realizing high-efficiency quantum dots solar cells (QDSC). InAs quantum dots (QDs) are grown using the Stranski-Krastenov growth mode which relies on strain, resulting from the mismatch between the InAs and the GaAs lattice parameters, to initiate three-dimensional growth. The generation of QDs does reduce the local strain but it is not completed alleviated. Therefore, as additional layers of InAs QDs are grown a significant tensile strain is built-up. During solar cell growth, this strain is naturally relieved by forming misfit boundaries and threading dislocations, which can damage the depletion region of the device. Strain relief is accomplished by growing the proper thickness of a compressively strained GaP, between each successive QD array. The strain localized at the InAs QD / GaAs interface is still present, allowing for QD growth but the net stress on the stack becomes zero, eliminating defect generation. Figure 1a contains a schematic of the baseline GaAs *pin* device and the strain compensated InAs QD / GaAs solar cell that was investigated. In Figure 1b, a schematic illustrating the electronic levels of the various materials in the strain compensated device, along with the potential excitation mechanisms are depicted; the primary and secondary photon excitation, along with photon assisted and thermal assisted electron extraction are indicated. In the following report, the thermal and radiation tolerance of these devices, in reference to a baseline GaAs devices, will be presented.
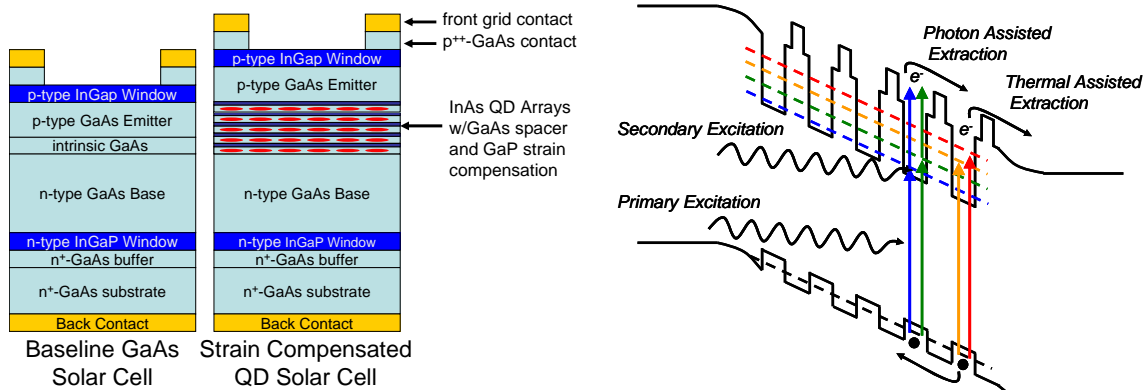
Figure 1. (a) Diagram depicting the baseline GaAs solar cell and the strain compensated QD solar cell structures. (b) Schematic depicting the energy bands of the strain compensated QD solar cell.

TABLE OF CONTENTS

Program Highlights

I. Thermal Behavior of Quantum Dot Solar Cells.

The thermal dependence of the QDSC, in relation to the baseline GaAs device, was invested by monitoring the current-voltage response of the device under dark and simulated AM0 illumination conditions while varying the temperature over the range of 80 K – 400 K. The spectral response was monitored in the same manner. The saturation current and ideality parameters were extracted from the dark current measurements assuming an ideal diode relationship. The dark current data for the two devices in addition to the variation in ideality and saturation currents with temperature are plotted in Figure 2a-d. This figure clearly illustrates that the thermal behavior of the QDSC is comparable to that of the baseline device response. Although the idealities parameters are slightly different (which could have been caused by cleaving the cells, poor contacts within the cryostat, etc.), the variation of this parameter with temperature is nearly identical for both devices. Furthermore, the saturation currents follow similar trends which can almost entirely be attributed to the temperature dependence of GaAs bandgap. There is a slightly larger variation with temperature in the saturation current of the QDSC device but this is very minor. Furthermore, the very low saturation current observed at <150 K may be related to the wide-bandgap GaP layers which could reduce the carrier thermalization within the junction and hinder the transport of thermalized carriers through the junction.
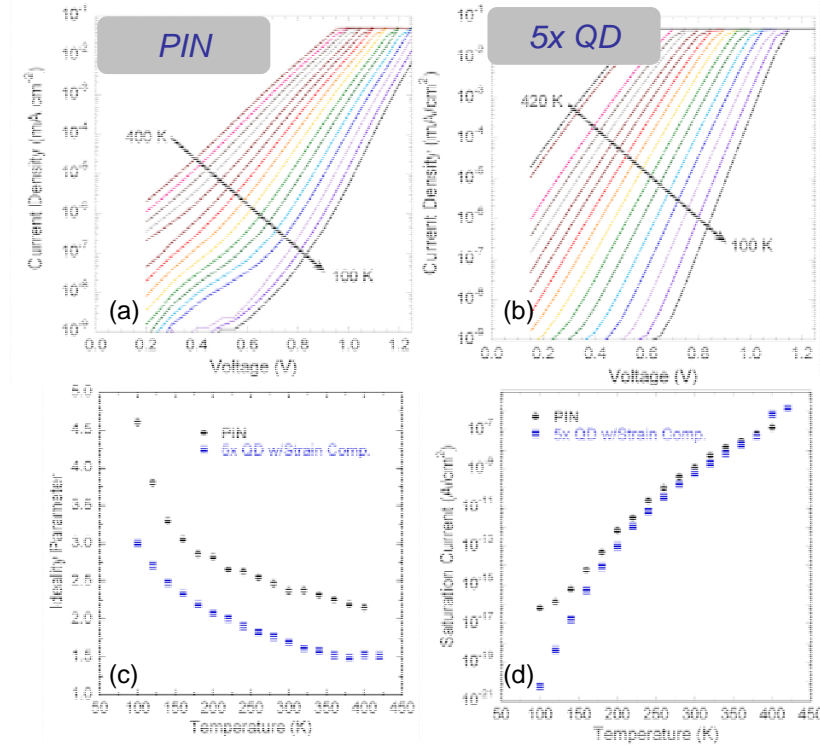

Figure 2. (a) Dark current-voltage response of baseline device and (b) the QDSC device over the temperature range of 100 K – 400 K.(c) and (d) Extracted ideality and saturation currents as a function of temperature for the baseline device and the QDSC device, respectively.

The AM0 illuminated current-voltage response of the two devices is depicted in Figure 3a-b. These two devices again demonstrate similar temperature dependences, the main difference being the lower open circuit voltage observed in the QDSC device. There is a slightly greater slope in the V_{oc} of this device which is the result of the slightly greater saturation current increase with temperature observed in the dark characteristics of the device. As expected, the spectral response of the devices showed nearly identical responses in the region of the spectrum which corresponds to phonons with energy greater than the GaAs bandgap (not shown).
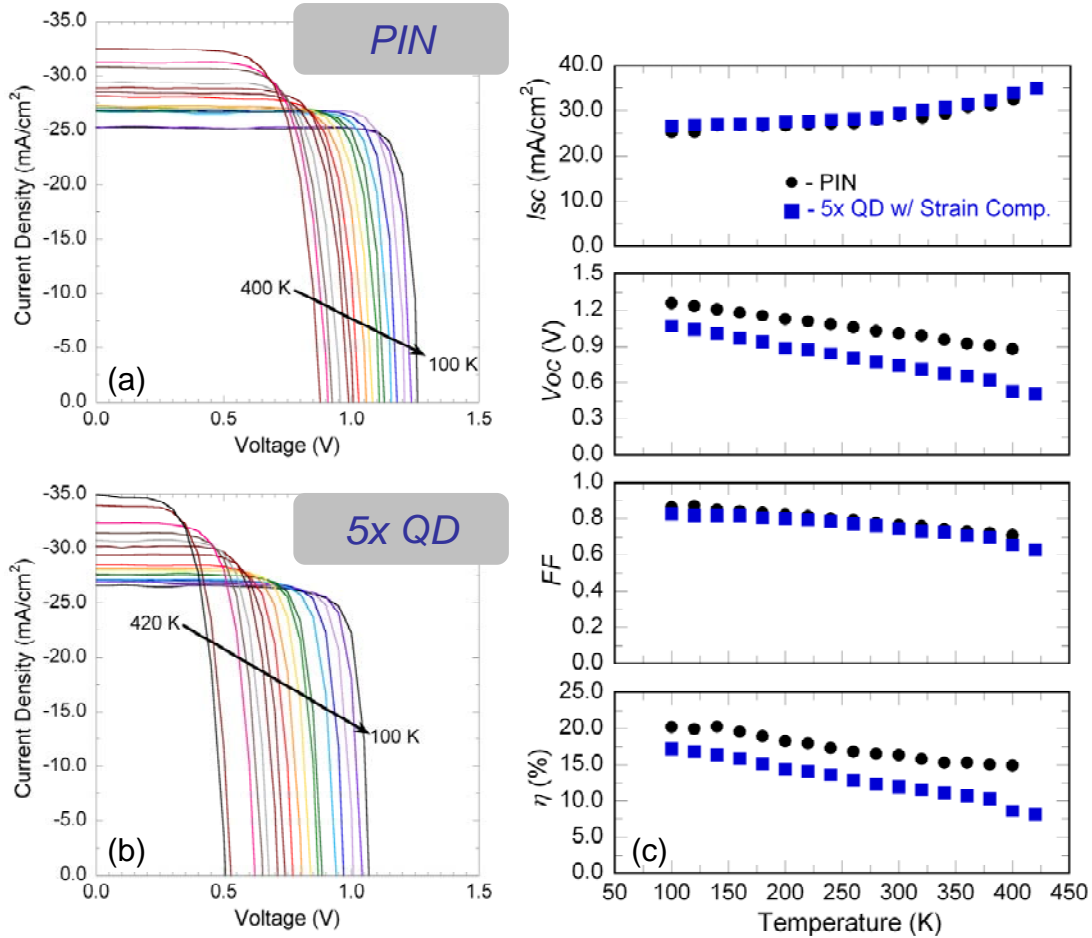

Figure 3. (a) and (b) contain the current-voltage response of the baseline GaAs device and the QDSC device, under simulated AM0 illumination, over the temperature range of 100 K – 400 K, respectively. The summary data for these measurements are provided in part (c).

The InAs QD spectral response variation with temperature is observable in the sub-gap response of the QDSC as illustrated in Figure 4a. Also included in this figure is the sub-gap response of the baseline device at 100 K and 420 K, which envelop the QDSC device response at shorter wavelengths. At longer wavelengths the InAs QD photoconversion can be observed and in particular, multiple peaks are present (labeled E1-E3) which result from the excited QD states or mini-band states within the InAs QD 5-layer stack. The electroluminescence, in Figure 4b illustrates the variation in the ground state, E1, of the InAs QD array with temperature. This emission is the result of

5

injecting carriers into the junction of the device, a total current of 200 mA/cm^2 was applied. The alignment of the electroluminescence with that of the spectral response of the device confirms that the response observed at these wavelengths is the result of the QDs. Interestingly, the intensity of the electroluminescence greatly reduces as the temperature is increased (over 4 orders of magnitude in going from 100 K – 420 K) meaning carriers are able to transit the junction without recombining, or other recombination mechanisms dominate their lifetimes. Based on the observed reduction in electroluminescence, one may expect an increase in the spectral response at the same wavelengths if the carriers are being extracted through thermalization. Such an increase is not observed in the spectral response of the QDSC device as temperature rises, which suggests that carrier thermalization is not the primary mechanism of carrier extraction.
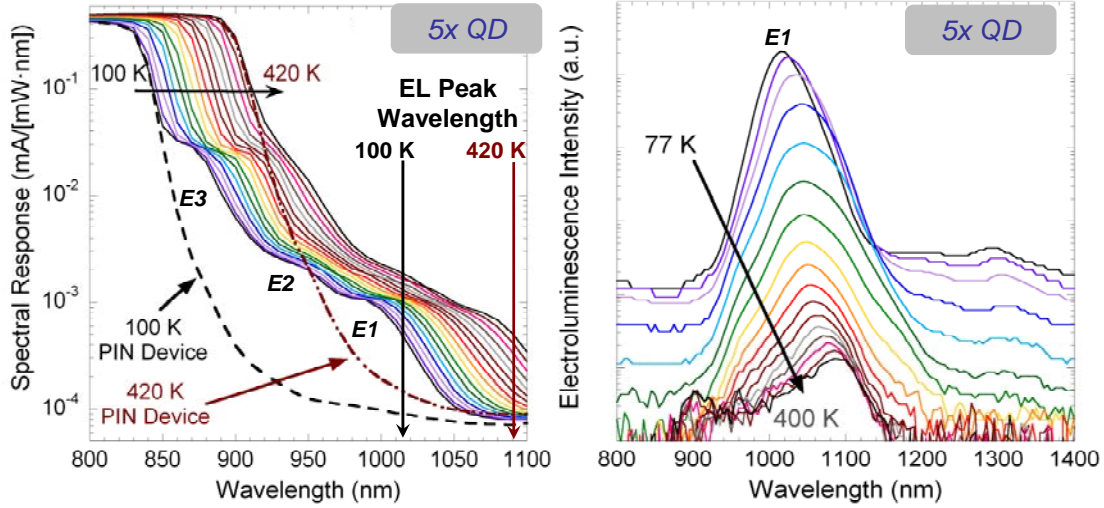
Figure 4. (a) Spectral response of the QDSC over the sub-GaAs bandgap range depicting the variation in the InAs QD response with temperature. For comparison, the 100 K and 420 K spectral response of the baseline GaAs device have been overlaid as dashed and dot-dash lines and the location of the electroluminescence peak emission are included. (b) The variation in the electroluminescence spectrum of the QDSC over the temperature ranging from 77 K – 400 K.

6

II. Radiation Effects on Quantum Dot Solar Cells.

The radiation response the two devices were investigated by measuring the room temperature spectral response and the current-voltage characteristics (AM0 illumination) as a function of alpha-particle irradiation. The irradiation source was a 1 mCi ^{210}Po alpha-particle emitter with an area of ~2.5 cm^2. The variation of the two devices in the visible region is very similar, wherein a greater rate of reduction is observed in the longer-wavelength region of the spectra (see Figure 5a,b). This suggests that the lifetime (and diffusion length) of holes in the base is reduced by the radiation induced defects making it less probable for them to diffuse to the junction when generated deep within the base.
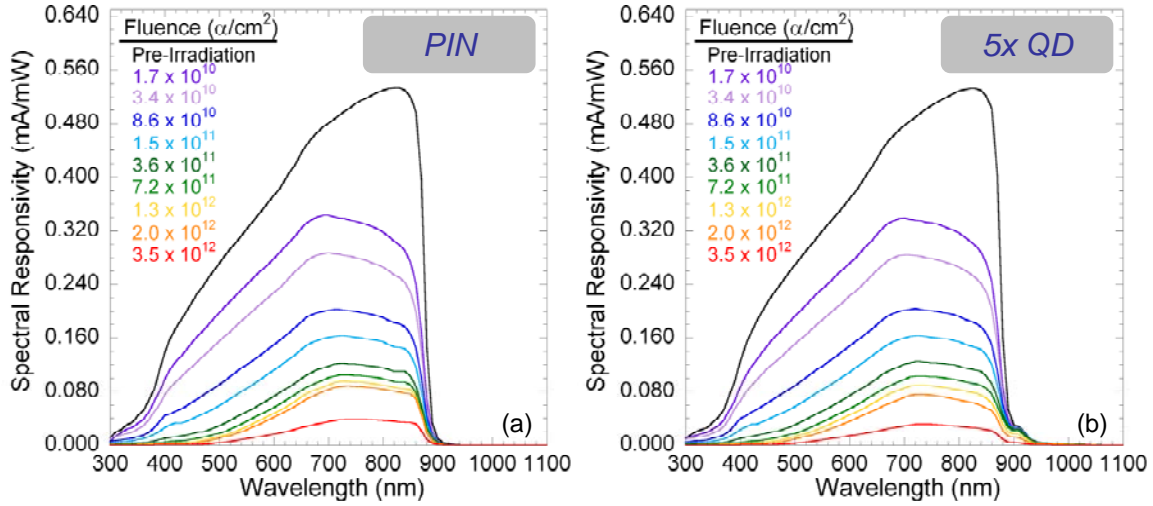

Figure 5. Spectral response spectra for (a) the baseline device and (b) the QDSC device for various levels of alpha-particle fluence.

The sub-gap region of the QDSC spectral response for increasing levels of fluence are depicted in   Figure 6a, along with the pre-irradiation and post 3.5 x 10^{12} alpha-particles / cm^2 spectral response curves for the baseline device. Pre-irradiation, the two devices demonstrate very similar spectral responses up to ~880 nm at which point the response of the baseline device drops towards zero, while the response of the QDSC is maintained as a result of the InAs QDs. For low-levels of fluence, the peak InAs QD response peak shows little variation, but at very high fluences, it does decline significantly. Although the InAs QDs can be damaged by the alpha-particles, generation of defects within the GaAs barriers and the subsequent junction degradation will inherently contribute to the degradation observed in the measured spectral response data. Even with these combined affects, the InAs QD degradation rate is much lower than that of the bulk GaAs. This may be the result of the stain within the InAs QDs, which has previously been shown to increase the energy threshold necessary to create a lattice defect within an InAs QD. The increased V_{oc} observed in the strain compensated QDSC, over that of the non-compensated QDSC device previously investigated, suggests that the concentration of defects within the junction has been significantly reduced by the strain compensation layers. It was originally suggested that the presence of such defects could reduce the rate of degradation in the device. Based on the current device performance, it

appears that the defects were not the main contributor to the radiation tolerance observed in that device. Figure 6b contains the spectral response as a function of fluence measured at 830 nm both devices and at 910 nm for the QDSC, which better illustrates the high tolerance observed in the InAs QD portion of the spectra.
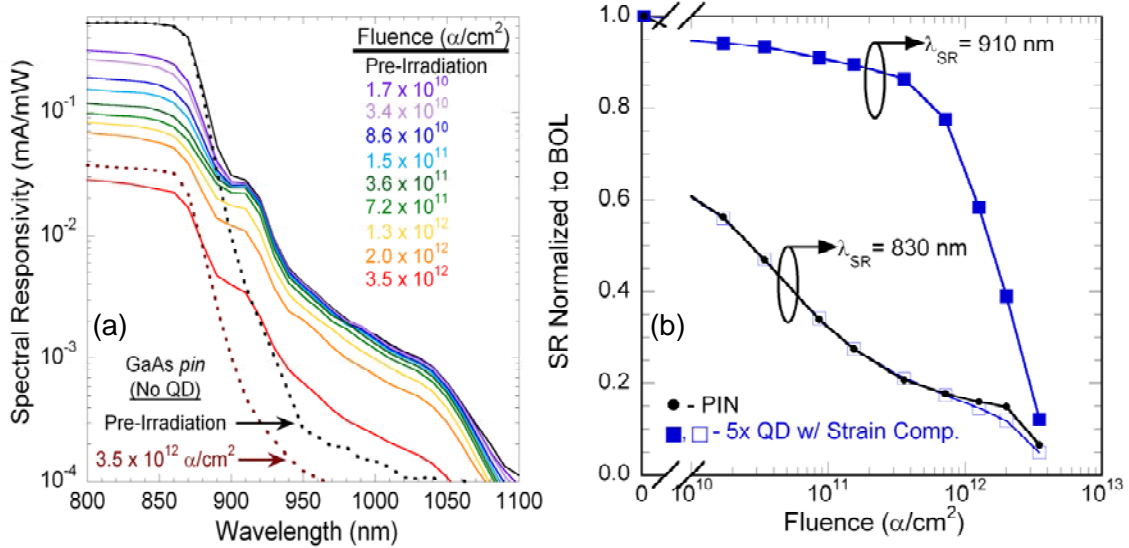

Figure 6. (a) Spectral response of the QDSC at incremental levels of alpha-particle fluence; the pre-irradiation and post 3.5 x 1012 alpha-particle/cm2 response spectra of the baseline device are overlaid for comparison. (b) The spectral response as a function of fluence measured at 830 nm for both devices and at 910 nm for the QDSC.

The variations in the normalized I_{sc}, V_{oc}, FF, and Efficiency with fluence are provided in Figure 7, for the baseline and the QDSC devices. The QDSC maintains a much greater normalized V_{oc} as compared to the baseline devices which suggests that the QDs are improving the tolerance of the overall device not just in the sub-gap spectral response. This improved V_{oc} leads to a greater normalized efficiency than that of the baseline device until a fluence of ~1 x 10^{12} alpha-particles/cm^2, at which point both devices have degraded to less than 5% of their beginning-of-life efficiency. The noticeable difference observed in the two devices is the decreased normalized fill factor observed in the QDSC device. The fundamental cause of this is still under investigation.
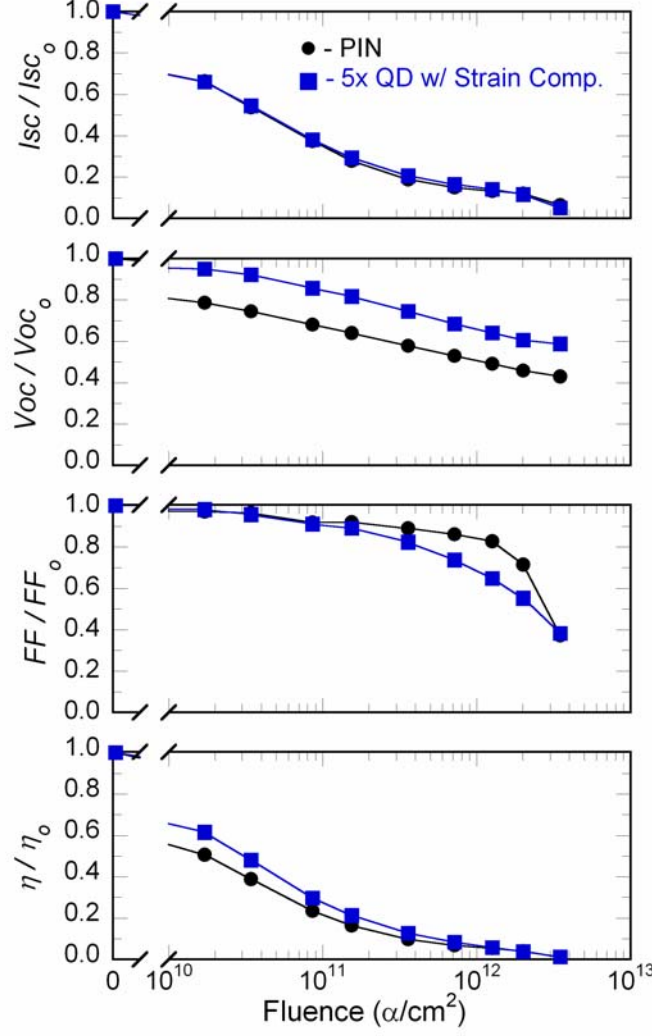
Figure 7. Normalized short circuit current, open circuit voltage, fill factor, and efficiency with alpha-particle fluence for the baseline and the QDSC devices.

In conclusion, similar the thermal and radiation dependence of a strain compensated InAs QD / GaAs solar cells have been invested in reference to a baseline GaAs device. The thermal dependence of the two devices is nearly identical and certainly within the sample-to-sample variation. Increased resilience in the V_{oc} and the sub-GaAs response of the QDSC was observed in the experimental results of the InAs QD /GaAs solar cell exposed to alpha-particle irradiation.

I. Modeling Radiation Damage using Tersoff Potentials

The probability and magnitude of the energy lost by irradiating particles to non-ionizing events is fundamentally dependent on the energy threshold for atomic displacement E_{th}. Historically, the determination of E_{th} has been performed experimentally whereby the rate of change in various material properties (*e.g.,* resistivity, carrier lifetime, etc.) is monitored with respect to the energy of irradiating electrons [1, 2]. An alternative approach for investigating E_{th} has been through the use of molecular

dynamic simulation. This technique dates back to the early 1960's when Vineyard and co-workers investigated the formation of defects in copper and iron [3, 4]. In general, the classical equations of motion are used to describe the behavior of hundreds of thousands of atoms. The interaction of the atoms is entirely dependent upon the lattice potential energy function; no assumptions are made regarding the structure of the material (except when initializing a simulation) or the nature of defects which may form by collision events. Initially all particles are at rest in a perfect lattice and the start of a radiation damage event is considered to be the sudden transfer of momentum to a PKO atom. The local potential energy then dictates the ability of an atom to be displaced as a result of the initial momentum transfer [3].

The accuracy of such simulations is entirely dependent upon the assumed potential energy function which dictates the magnitude and direction of forces controlling the motion of the PKO. The Lennard-Jones potential is a well known potential energy function consisting of 2-body pair potentials describing the attractive (ion-electron) and repulsive (ion-ion and electron-electron) forces associated with ionic materials [5]. This potential energy function favors the formation of close-packed structures, such as face centered cubic. To describe the diamond-like binding (*i.e.* zinc blend) associated with III-V semiconductors, three-body interactions terms are necessary. Potential energy functions which have been used to model III-V semiconductor bulk and nanomaterials include the Keating potentials [6], the valence force field method [7], the Stiller-Weber potentials [8], and the Tersoff potentials [9-11]

Tersoff interatomic potentials are analytically defined functions which describe 2-body and 3-body interactions of an N-body system. The inclusion of the 3-body interactions provides a means to stabilize more open structures such as diamond and zinc blend. The final component of the Tersoff model is a bond-order dependent attraction term which varies the strength per bond depending on the local environment of the atom. This results in a more realistic attractive potential (especially in partially ionic systems) and allows for non-equilibrium bonding (*e.g.*, bonds with atoms in interstitial sites) to be more accurately modeled. The Tersoff potentials have been used on many occasions to investigate the properties associated with GaAs and InAs materials. Some examples include the InGaAs/GaAs strained-layer relaxation process [12, 13] and the melting behavior of GaAs [14]. This set of potentials is ideal for investigating the effect that materials properties have on E_{th}.

The Tersoff potentials are defined by the following set of equations:

$$E_{eq} = \frac{1}{2} \sum_{j \neq i} f_c(r_{ij}) \left(V_{ij}^R(r_{ij}) + b_{ij} V_{ij}^A(r_{ij}) \right), \tag{1}$$

$$V^R(r_{ij}) = A_{ij} \exp(-\lambda_{ij} r_{ij}), \tag{2}$$

$$V^A(r_{ij}) = B_{ij} \exp(-\mu_{ij} r_{ij}), \tag{3}$$

$$b_{ij} = \left(1 + (\gamma_{ij} \zeta_{ij})^{n_i} \right)^{-n_i/2}, \tag{4}$$

$$\zeta_{ij} = \sum_{k \neq i,j} f_c(r_{ik}) g(\theta_{jik}) \exp\left(\lambda_o^3 (r_{ij} - r_{ik})^3 \right), \tag{5}$$

$$g(\theta_{jik}) = 1 + \frac{c_i^2}{d_i^2} - \frac{c_i^2}{d_i^2 + (h_i - \cos(\theta_{jik}))^2}, \tag{6}$$

10

$$f_c = \begin{cases} 1, r_{ij} < R_{ij}, \\ \frac{1}{2}\left(1 + \cos\left(\pi\left(r_{ij} - R_{ij}\right)/\left(S_{ij} - R_{ij}\right)\right)\right), R_{ij} < r_{ij} < S_{ij}, \\ 0, r_{ij} > S_{ij}; \end{cases} \qquad (7)$$

The total energy per atom, E_{eq} is found by summing the repulsive bond energy (2) and the attractive bond energy (3) between atoms i and j with interatomic spacing of r_{ij}. The cutoff function (7) is used to limit the neighbors j which affect the cohesive energy of atom i, the "focus" atom. Equations (4) – (6) are used to determine the aforementioned bond-order term which varies the level of the attractive potential depending on the number of atoms the focus atom is bonding with. The values of the variables used to parameterize the equations are free parameters which are obtained by fitting the equations to agree with empirical data.

Determining the full extent of damage caused by a particle-atom collision event requires the use of a fully dynamic simulation program to track the path of the PKO. In contrast, the determination of E_{th} can be performed using a static lattice since one is not concerned with the subsequent motion of the particle. However, for such a calculation to be physically meaningful, the movement of the PKO must be much faster than that of the thermal oscillations of the lattice. In other words, the PKO must be moving so fast that the lattice "appears" to be standing still. Provided this condition is met, the E_{th} can then be found by calculating the energy of the focus atom (PKO) at sites within the lattice at a distance dr from the equilibrium lattice location. The maximum energy encountered along a path prior to reaching a local energy minimum (interstitial site) is the E_{th} in that direction. Performing this calculation along all (unique) paths allows one to find the true E_{th} for a material. This methodology is used to determine the E_{th} of In and As atoms within an InAs lattice. The affects of strain on these values is also investigated.

As discussed above, the threshold energy for atomic displacement E_{th} dictates the level of non-ionizing damage that will be incurred by a semiconductor under irradiation. Just a small increase in E_{th} has a large effect on the total number of defects generated by a particle because the energy lost by the particle to the PKO and all subsequent collision events the PKO has with neighboring atoms requires more energy to create a defect. For instance, increasing the E_{th} of In and As atoms from 4.0 eV to 4.5 eV in a SRIM simulation of 5 MeV alpha-particles in InAs reduces the number of vacancies per alpha-particle from ~1800 to ~1650 [15, 16]. This corresponds to a reduction in vacancy generation by over 8%. The observed enhancement in radiation tolerance of the InAs QDs within the GaAs solar cells, therefore, suggests that there may be some physical property that is increasing the E_{th} within this material system. Besides the smaller size, the main property associated with these materials is the large compressive strain field which exists within the QDs [17-19]. With the use of the Tersoff interatomic potentials, the effect that a compressive strain field has on E_{th} is investigated.

This investigation is initiated by populating an InAs lattice with In and As atoms situated at their equilibrium positions, corresponding to a lattice parameter of 6.058 Å (see Figure 8a) [12]. An In or As atom is chosen as the PKO situated at the (0,0,0) lattice position and the cohesive energy of the atom situated at this site is calculated by summing over the neighboring bonds as defined by the Tersoff potential model. A value of -3.107 eV is obtained which is consistent with the literature values [12-14]. As

depicted in Figure 8b-f, the atom is then stepped throughout the lattice and at each point the cohesive energy of the atom is re-calculated. Initially, the goal is to determine the location of the interstitial sites, and the energy associated with those sites. An interstitial site may be defined as a local potential energy minimum, and can be found by plotting equi-potential surfaces with increasing energy. As depicted in Figure 9 the interstitial sites surround the basis atom situated at the (a/4, a/4, a/4) lattice position. In this figure the interstitial sites for an As atom in the InAs lattice are depicted. A similar result is obtained for In although the energy and location of the sites are different. Differences arise because the In-In and As-As bonding have different energies associated with them.
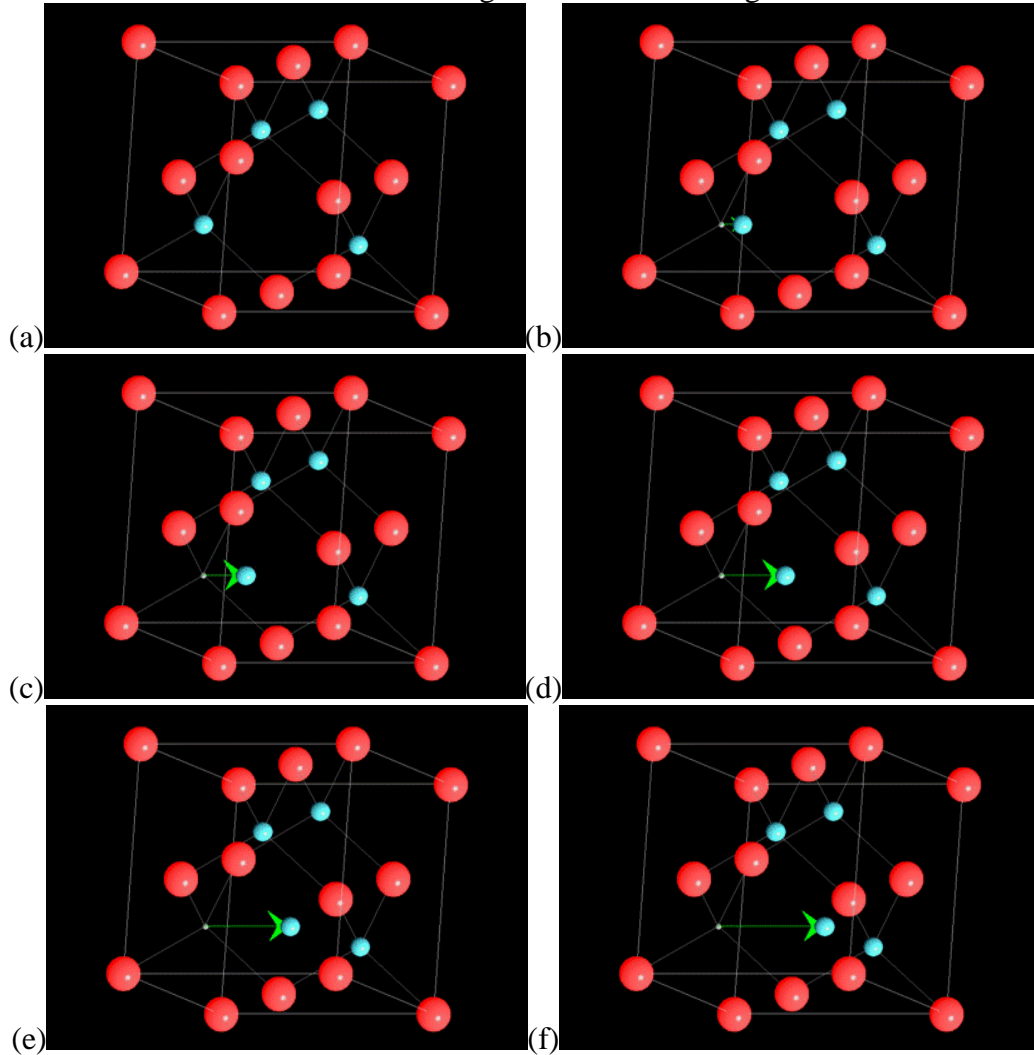

Figure 8. (a) Zincblend bonding structure of InAs, where In and As atoms are represented by blue and red spheres, respectively. (b)-(f) Depictions of the simulation process where an In (As) is displaced from its equilibrium bonding sight into points locations within the lattice. At each displacement, the potential energy of the atom is calculated.
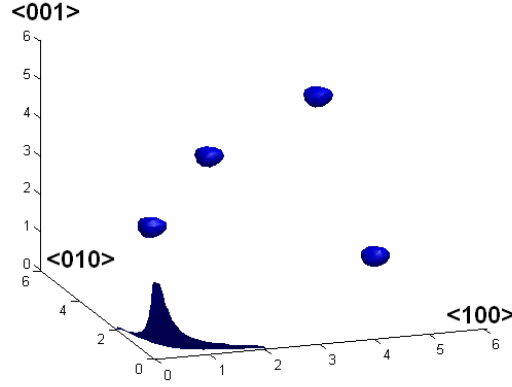
Figure 9. Equi-potential surfaces indicating the locations of local minima for As within the InAs lattice. Moving from left to right, the four blue spheres correspond approximately with the following crystal locations (x,y,z) = (a/4,3a/4,a/4), (a/4,a/4,3a/4), (3a/4,3a/4,3a/4), and (3a/4,a/4,a/4). The surface near (0,0,0) corresponds to the top of the well (in energy) that the atom sits when in its equilibrium position. An In atom is located at (a/4,a/4,a/4) and therefore these four interstitial sites surround that atom.

The threshold for displacement for a given direction, $E_{th,r}$, where r is the displacement vector, is now defined as the maximum energy encountered along r before reaching a local minimum. For example, the black trace in Figure 10 depicts the potential energy of an In atom as it is displaced along the (201) direction towards an interstitial site near (a,0,a/2). Along this path, the atom approaches the face atom on the (100) plane, this causes the energy of the atom to peak at a displacement of ~ 4.2 Å before reaching the interstitial site. The difference between the peak energy and the energy of the atom at the equilibrium bonding site corresponds to the $E_{th,r}$ for this particular value of r.
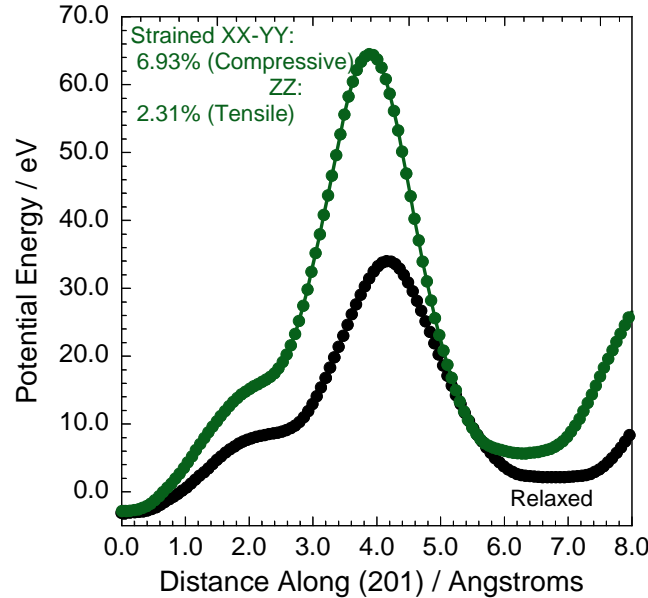

Figure 10. Potential energy of an Indium PKO along r = (201) for a relaxed InAs lattice (black trace) and a strained lattice (green trace).

Figure 10 also contains a trace depicting the effect of strain on the potential energy encountered by the atom along the same path. To simulate a strained InAs lattice, a compressive strain of ~7% in the x and y directions was assumed based on the

difference in lattice parameters between InAs and GaAs. Additionally, the compressive strain in the x and y directions will cause the lattice to expand in the z-direction and for that a Poisson's ratio of 1/3 was assumed yielding a tensile strain of ~2.3 % in the z-direction. Strain has a profound effect on the $E_{th,r}$, along this direction. It is increased by over a factor of 2, and the energy of the interstitial site is also increased.

The above example illustrates the large affect that strain has on the threshold energy for displacement. However, the strain in quantum dots is not constant; theoretical calculations have shown predicted the strain to range from a maximum of ~7% compressive at the base of the quantum dot and slowly relax becoming slightly tensile at the peak (this was predicted for pyramidal InAs QDs on GaAs [17]). The effect of strain on the cohesive (potential) energy of the atom occupying its equilibrium site is depicted in Figure 11. As expected, the equilibrium energy increases with increasing strain indicating that the lattice is no longer arranged in the minimum energy configuration.
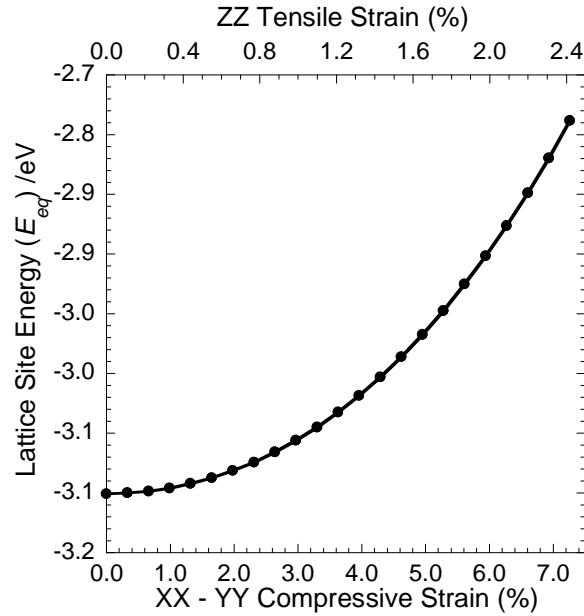

Figure 11. Effect of strain on the equilibrium lattice cohesive energy of the atom.

Furthermore, the effect of varying the strain on the knock-out energy lower bound for In and As PKOs reaching the specified interstitial site are depicted in Figure 12a and b, respectfully. In both cases increasing strain results in a slightly non-linear increase in the lower bound on the $E_{th,r}$ which is defined as the difference between the interstitial site energy and the equilibrium bonding site energy. This means the energy associated with the atoms occupying interstitial sites increases a greater rate than that of the (0,0,0) site energy depicted above. This is considered the lower bound on the $E_{th,r}$ because it is the minimum amount of energy required to force the PKO into the interstitial location while still conserving energy.
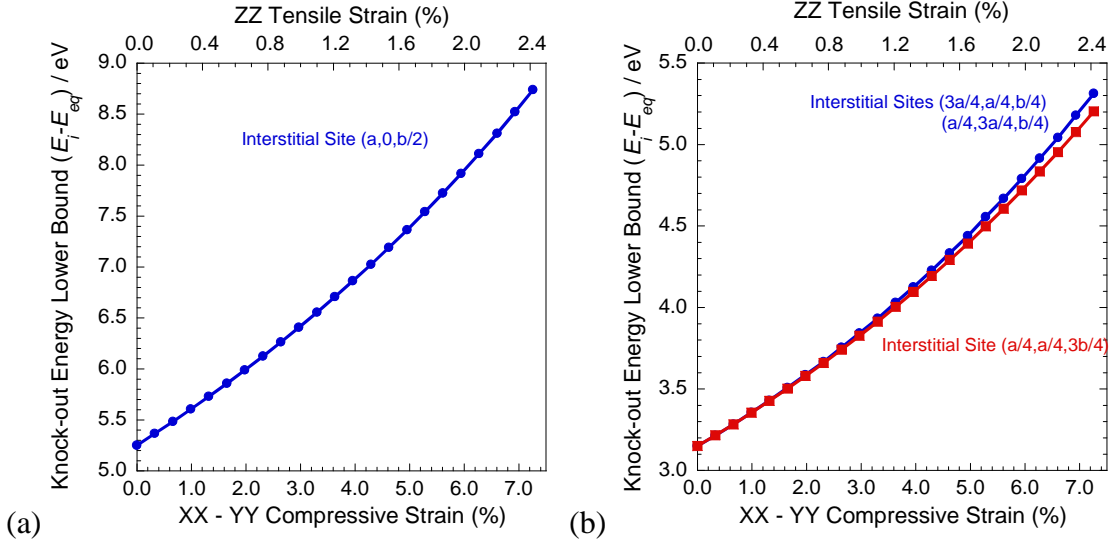
Figure 12. Effect of strain on the minimum knock-out energy required to reach the labeled interstitial sites for (a) In and (b) As as the PKO.

The above results have provided convincing arguments that strain has a large impact on the minimum energy to displace an atom. However, to determine the actual E_{th}, which is the minimum of all $E_{th,r}$, the peak energy encountered by a PKO along all possible directions must be considered. A methodology for performing is calculation is described here. To begin, a spherical coordinate system (r, ϕ, θ) is employed for the displacement of the atoms within the lattice. This allows all unique directions in the lattice to be investigated simply by varying ϕ and θ over π and $\pi/2$, respectively. For each set of ϕ and θ, the PKO is translated linearly along r. To determine the $E_{th,r}$ a criteria can then be defined. For illustrative purposes, the following criteria have been chosen. First, the atom must be at a location which is beyond one interatomic spacing distance from the (0,0,0) site. This eliminates the possibility that un-stable defects (local minima) near the (0,0,0) are chosen. Secondly, the peak energy is then defined as the maximum energy encountered prior to a reduction in potential energy after reaching one interatomic distance from the (0,0,0) site. Many different criteria may be chosen for in this methodology depending on the type of irradiating particle and the expected amount of energy imparted to the PKO.

An example of the results which can be obtained from this methodology is depicted in Figure 13. This figure contains a contour plot of the log of the minimum displacement energy $(E_{th,r})$ as a function of ϕ and θ direction for an In PKO in InAs. Also listed on the plot are the typical lattice directions which correspond to single points on this figure. For example, the [100] corresponds to the point $\phi = 0$ and $\theta = 90$ point. Along this direction there is an atom situated one lattice parameter away and therefore the figure is red in this directing indicating that a large potential energy is required to cause a displacement. A similar trend is observed for all traditional lattice directions, wherein a red region indicates the presence of an atom along that path (at least within the first lattice cell). Also apparent in the figure is a drastically different potential energy profile encountered depending on whether the PKO is directed towards the positive or negative y-direction (*i.e.,* positive or negative ϕ). In the positive ϕ direction the basis atom of the PKO is nearby, situated at the (a/4,a/4,a/4) lattice site. This atom greatly limits the ability

15

of the PKO to be displaced into this octant of the lattice, except for displacements surrounding this atom. This is consistent with the results depicted in Figure 9 above, where the locations of the interstitial sites surround this basis atom. In the negative φ direction the situation is reversed. The atom can easily be displaced in the [1 $\bar{1}$ 1] but encounters neighboring atoms surrounding those directions. These results provide theoretical evidence confirming the experimentally observed anisotropic defect introduction in GaAs in which it was shown that there is an "easy" and a "hard" [111] direction for displacement of Ga and As within GaAs [20]. The abrupt variation in the threshold energy that is observed when crossing from the negative to positive φ region of the contour plots is a consequence of the interstitial sites in these locations being at different radial distances from the equilibrium position.
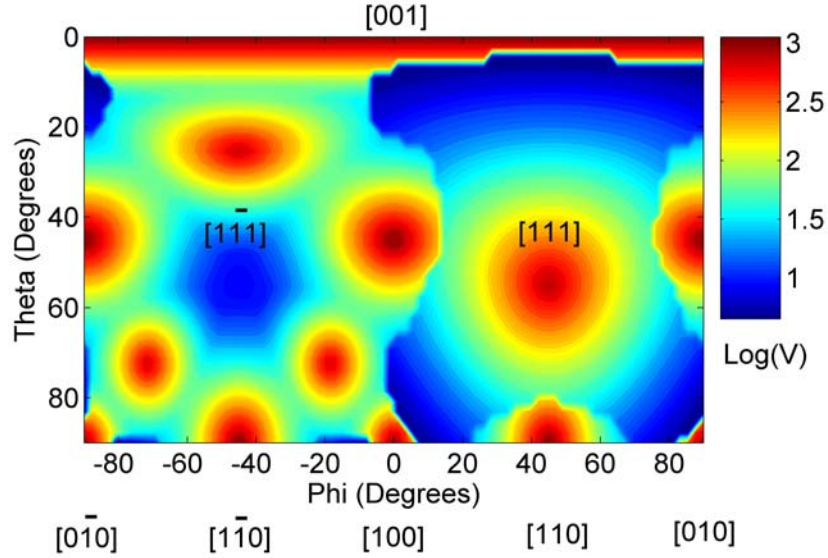

Figure 13. Contour map depicting the log of the minimum energy for displacement along direction (φ, θ) for an In PKO in relaxed InAs.

The effects of strain on minimum energy displacement for In in an InAs lattice under ~7% in-plane compressive strain along with the associated z-directed 2.3% tensile strain is depicted in Figure 14. The tensile strain in the z-direction is immediately evidenced by the larger blue region directed above the [111]. Furthermore, the shape of the minimum energy direction near the [1 $\bar{1}$ 1] appears to be deformed, resembling a slight rotation, and the exact locations of the red regions "atoms" have shifted from their corresponding location on the relaxed contour plot.
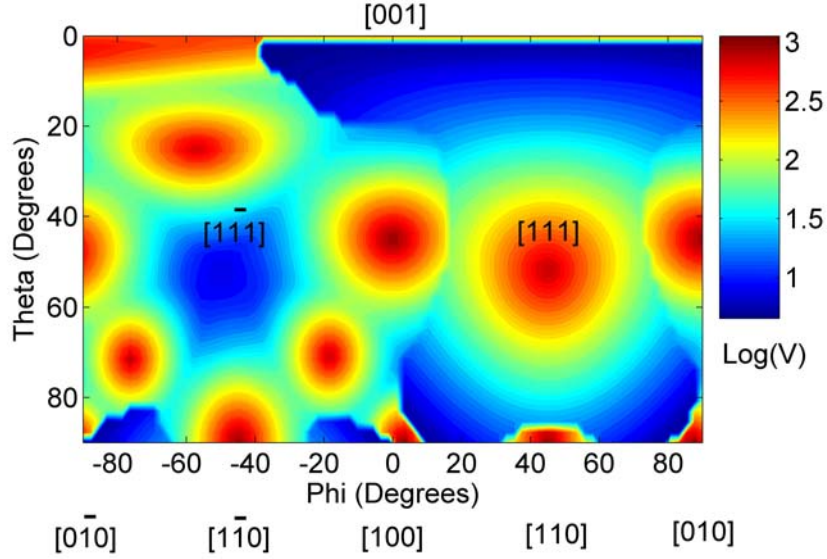
Figure 14. Contour map depicting the log of the minimum energy for displacement along direction (ϕ, θ) for an In PKO in InAs under ~7% xx-yy compressive strain and ~2.3% zz tensile strain.

Besides structural information, data regarding the E_{th} can also be ascertained from this methodology. Taking the minimum energy of all points associated with each of the above two figures yields E_{th} values of 3.75 eV and 4.53 eV, respectively. This corresponds to an increase in over 0.75 eV per vacancy generation which corresponds to a reduction in vacancies generated by irradiation alpha particles more than 10%. Similar results are obtained for As when comparing the strained and relaxed lattices. Simulations in which the criteria was set to find the maximum energy encountered along a translation of 10.5 Å yielded E_{th} values of 16.48 eV and 19.12 eV for the relaxed and strained InAs cases, respectively. These result supports the theory that the increased radiation tolerance observed in InAs QDs grown on GaAs is fundamentally linked to strain induced increases in E_{th} for In and As PKOs.

Publications

This work has resulted in the 4 journal and conference proceeding publications listed below. This work has also resulted in presentations at the Photovoltaics Specialists Conference, Space Photovoltaics Research and Technical Conference, and the Material Research Society.

(1) Quantum dot solar cell tolerance to alpha-particle irradiation. Cress, Cory D.; Hubbard, Seth M.; Landi, Brian J.; Raffaelle, Ryne P.; Wilt, David M. Applied Physics Letters (2007), 91(18), 183108/1-183108/3.

Abstract
The effects of alpha-particle irradiation on an InAs quantum dot (QD) array and GaAs-based InAs QD solar cells were investigated. Using photoluminescence (PL) mapping, the PL intensity at 872 and 1120 nm, corresponding to bulk GaAs and InAs QD emissions, respectively, were measured for a five-layer InAs QD array which had a spatially varying total alpha-particle dose. The spectral response and normalized current-

voltage parameters of the solar cells, measured as a function of alpha-particle fluence, were used to investigate the change in device performance between GaAs solar cells with and without InAs QDs.

(2) Radiation and Thermal Behavior of III-V Quantum Dot Space Solar Cells
Cory D. Cress, Seth M. Hubbard, Ross E. Robinson, and Ryne P. Raffaelle, David M. Wilt and Sheila G. Bailey. Proceedings of the 20th Space Photovoltaics Research and Technology Conference, Cleveland, OH, Sept. 25-27, 2007.

Abstract
The temperature dependent current density vs. voltage (dark and illuminated) and spectral response were measured for GaAs-based p-type / intrinsic /n-type (*pin*) solar cell devices containing 1- and 5-layers of InAs quantum dots. The dark diode measurements revealed the predominate forward current components (i.e., injection, space charge region recombination, and tunneling) of the devices.   Illuminated current density Vs voltage measurements were used to determine the temperature coefficients of the open circuit voltage, short circuit current, maximum power, and fill factor. Devices were subjected to 4.2 MeV alpha-particle irradiation and the variations in the maximum power output and the spectral response at wavelengths above and below the GaAs bandgap were monitored as function of fluence. The spectral response in the region below the GaAs bandgap (i.e., >870 nm), relating to the QD photocurrent generation, demonstrated a much greater resilience to radiation damage as compared to the spectral response of the device above (<870 nm) the GaAs bandgap.

(3) Thermal Dependence of Quantum Dot Solar Cells. C.D. Cress, S.M. Hubbard, R.E. Robinson, C.G. Bailey, B.J. Landi, and R.P. Raffaelle, Prodeedings of the Materials Research Society Fall 2007 Symposium: Boston, MA, 2007 (MRS); Paper H13.19.

Abstract
Various temperature dependent optoelectronic properties were measured for GaAs-based p-type / intrinsic / n-type (*pin*) solar cell devices containing 5-layers of InAs quantum dots (QDs) grown with strain-compensation layers. Curve fitting of the dark diode characteristics allowed for the temperature dependence of the saturation current and the ideality parameter to be determined. The resulting parameter values indicate high material quality. Air mass zero illuminated current density vs. voltage measurements were used to determine the temperature coefficients of the open circuit voltage, short circuit current, maximum power, and fill factor. A strong correlation between the temperature dependent quantum dot electroluminescence peak emission wavelength and the sub-GaAs bandgap spectral response was observed.

(4) Radiation Effects on Strain Compensated Quantum Dot Solar Cells. Cory D. Cress, Seth M. Hubbard, Ross E. Robinson, and Ryne P. Raffaelle, David M. Wilt and Sheila G. Bailey. To be presented at the 33rd IEEE Photovoltaic Specialists Conference, San Diego, CA, May 11-16, 2008.

Abstract

The dependence of satellites on solar cell power systems has continually fueled the development of increased efficiency and radiation resistance devices. The incorporation of quantum dots (QDs) into traditional single or multi-junction crystalline solar cells is a potentially advantageous means for improving the overall conversion efficiency and radiation tolerance of these devices. The effects of alpha-particle irradiation on the current-voltage characteristics and spectral response of GaAs-based p-type / intrinsic / n-type solar cell devices containing 5-layers of InAs quantum dots grown with strain-compensation layers were investigated. The devices were subjected to ~4.2 MeV alpha-particle irradiation and the variation in the air mass zero short circuit current, open circuit voltage, fill factor, efficiency, and spectral response were monitored as function of alpha particle fluence and displacement damage dose. The spectral responses at wavelengths above and below the GaAs bandgap were used to investigate the rate of degradation in the InAs QDs in comparison to that of the bulk GaAs. A computation model was used to study the effects of strain on the knock-out energy for the atoms within an InAs QD. Using the many body Tersoff potentials, the energy of the primary knock-on atom occupying various sites within the lattice was calculated as a function of strain. The observed increases in minimum knock-out energy and interstitial-site energy with strain suggest a potential mechanism for the increased radiation tolerance observed in Stranski-Krastanow grown QDs.

References

[1]   H. Flicker, J. J. Loferski, and J. Scott-Monck, *Physical Review*, **128**(**6**), 1962, pp. 2557.

[2]   J. J. Loferski and P. Rappaport, *Physical Review*, **111**(**2**), 1958, pp. 432.

[3]   C. Erginsoy, G. H. Vineyard, and A. Englert, *Physical Review*, **133**(**2A**), 1964, pp. A595.

[4]   C. Erginsoy, G. H. Vineyard, and A. Shimizu, *Physical Review*, **139**(**1A**), 1965, pp. A118.

[5]   C. Kittel, *Introduction to Solid State Physics*, 7th ed: John Wiley & Sons, Inc., 1996, pp. 673.

[6]   P. N. Keating, *Physical Review*, **145**(**2**), 1966, pp. 637.

[7]   M. J. P. Musgrave and J. A. Pople, *Proc. Roy. Soc.*, **474**, 1962, pp. A268.

[8]   F. H. Stillinger and T. A. Weber, *Physical Review B*, **31**(**8**), 1985, pp. 5262.

[9]   J. Tersoff, *Physical Review Letters*, **56**(**6**), 1986, pp. 632.

[10]   J. Tersoff, *Physical Review B*, **37**(**12**), 1988, pp. 6991.

[11]   J. Tersoff, *Phys. Rev. B.*, **39** (**8**), 1989.

[12]   P. A. Ashu, J.H.Jefferson, A.G.Cullis, W. E. Hagston, and C. R. Whitehouse, *J. Crystal Growth*, **150**, 1995, pp. 176-179.

[13]   M. A. Migliorato, A. G. Cullis, M. Fearn, and J. H. Jefferson, *Phys. Rev. B.*, **65**, 2002, pp. 115316.

[14]   K. Albe, K. Nordlund, J. Nord, and A. Kuronen, *Physical Review B*, **66**(**3**), 2002, pp. 035205.

[15]   J. F. Ziegler, *J. Appl. Phys. / Rev. Appl. Phys.*, **85**, 1999, pp. 1249-1272.

[16]   J. F. Ziegler, J. P. Biersack, and U. Littmark, *The Stopping and Range of Ions in Solids*, vol. 1. New York: Pergamon Press, 1985.

[17]   D. Bimberg, M. Grundmann, and N. N. Lednetsov, *Quantum Dot Heterostructures*, vol. 1. Chichester: John Wiley and Sons, 1999.

[18]   S. M. Hubbard, R. P. Raffaelle, R. Robinson, C. Bailey, D. M. Wilt, D. Wolford, W. Maurer, and S. Bailey, "Growth and Characterization of InAs Quantum Dot Enhanced Photovoltaic Devices," *Proceedings of Proc. of the Materials Research Society Spring Meeting*, 2007.

[19]   S. M. Hubbard, D. M. Wilt, S. Bailey, D. Byrnes, and R. P. Raffaelle, "OMVPE Grown InAs Quantum Dots for Application in Nanostructured Photovoltaics," *Proceedings of Proc. of the World Conference on Photovoltaic Energy Conversion*, 2006, 118-121.

[20]   D. Pons and J. Bourgoin, *Physical Review Letters*, **47**(**18**), 1981, pp. 1293.